Sea Ice Motion Vector Retrievals from AMSR2 89-GHz Data: Validation Algorithm with Simultaneous Multichannel Observations

ERI YOSHIZAWA,[a] TAKASHI KAMOSHIDA,[b] AND KOJI SHIMADA[c]

[a] *Earth Observation Research Center, Japan Aerospace Exploration Agency, Tsukuba, Ibaraki, Japan*
[b] *AquaSound Inc., Kobe, Hyogo, Japan*
[c] *Department of Ocean Sciences, Faculty of Marine Science, Tokyo University of Marine Science and Technology, Tokyo, Japan*

(Manuscript received 16 May 2022, in final form 14 September 2022)

ABSTRACT: In retrievals of sea ice motion vectors (SIMVs) based on passive microwave observations, the use of the high-resolution 89-GHz channel of the Advanced Microwave Scanning Radiometer 2 (AMSR2) has the advantage of enhancing the theoretical precision of correlation-based motion tracking. However, its higher sensitivity to atmospheric moisture than lower-frequency channels links maximum cross-correlation peaks to outlier vectors and obscures signals of valid vectors. This study develops an algorithm to select valid vectors from candidates detected by multiple cross-correlation peaks based on validations with large-scale sea ice displacements extracted from 19- and 37-GHz data after questionable vectors are prefiltered by comparing them with reanalysis surface wind and neighboring vectors. The algorithm selects a vector corresponding to large-scale motion as the optimal vector. The retrieved results from 2013 to 2020 show that by replacing outlier vectors with valid ones detected by second or third cross-correlation peaks, validation with simultaneous observations enables retrieval of more than 60% of the Arctic motion field from 89-GHz data in winter but only 10% in summer; therefore, lower-frequency data are employed for retrievals. The uncertainty assessment using in situ data from acoustic measurements from ocean moorings shows that the algorithm provides daily SIMVs with root-mean-square errors of only 1–2 cm s^{-1} in idealized winter conditions with the absence of diurnal brightness temperature (Tb) changes that make tracking of the similarity of Tb fields difficult. The analysis also illustrates the applicability limit of the algorithm for summer retrievals.

SIGNIFICANCE STATEMENT: An algorithm was developed to validate sea ice motion vectors retrieved from AMSR2 89-GHz data by those from lower-frequency data. The validation via simultaneous observations enabled that valid vectors are sorted from invalid ones resulting from weather effects.

KEYWORDS: Ocean; Arctic; Sea ice; Algorithms; Microwave observations; Satellite observations

1. Introduction

The sea ice motion vector (SIMV) is a fundamental physical parameter to quantify air–ocean momentum transfers in the polar climate system. Despite its importance, in situ observations have been limited in time and space due to severe climatic conditions. Thus remote-tracking techniques have been developed since the early satellite observation era, based on the maximum cross-correlation (MCC) method, which searches for matching patterns by calculating spatial lag correlations among pixel templates extracted from successive images obtained by satellite sensors: Advanced Very High-Resolution Radiometer (AVHRR; Ninnis et al. 1986; Emery et al. 1991), synthetic aperture radar (SAR; Emery et al. 1986), and passive microwave (PMW) radiometers (Agnew et al. 1997). Although the PMW sensors offer coarser spatial resolutions than the others, they can observe the sea ice cover across the Arctic/Antarctic Ocean daily. Additionally, they have provided long-term data records, enabling consecutive monitoring of basin-scale sea ice circulations over the past few decades. Therefore, PMW-derived SIMV is in great demand, not only for climatological research, but also for assisting assimilation and forecasting systems (Stark et al. 2008; Rollenhagen et al. 2009).

The MCC method is robust from methodological and computational points of view but has the constraint that, as an image pixel size is upsized, the precision of motion tracking decreases (i.e., quantization noise increases). As the noise level becomes unacceptable for measuring sea ice motion when images with a typical PMW observation pixel size (a few tens of kilometers) are used, methodologies have been developed to reduce them; for example, by interpolating a cross-correlation function (Kwok et al. 1998), applying wavelet transform to image processing (Liu et al. 1999), and conducting a nonlinear optimization of displacement estimations (Lavergne et al. 2010). Oversampling of images has a similar effect on noise reduction. In this context, it is advantageous to utilize the Advanced Microwave Scanning Radiometer 2 (AMSR2) on board the *Global Change Observation Mission for Water* (*GCOM-W*), as well as its scheduled-for-launch successor (AMSR3), because they offer a factor of 2 higher spatial resolutions compared to other PMW sensors, such as the Special Sensor Microwave Imager Sounder (SSMIS) on board the U.S. Defense Meteorological Satellite Program (DMSP). Furthermore, the resolution increases as the observation

Denotes content that is immediately available upon publication as open access.

Corresponding author: Eri Yoshizawa, yoshizawa.eri@jaxa.jp

DOI: 10.1175/JTECH-D-22-0049.1

TABLE 1. Channels of AMSR2 used in SIMV retrieving. For the polarization, H is horizontal and V is vertical.

	Frequency (GHz)					
	18.7		36.5		89.0	
Polarization	H	V	H	V	H	V
Footprint resolution (km; cross- × along-track)	14 × 22		7 × 12		3 × 5	

frequency increases; particularly, the highest 89-GHz channel has a 3 km × 5 km footprint resolution in the cross- and along-track directions, which is comparable to that of AVHRR. This suggests a great possibility for improving the accuracy and resolution of PMW-derived sea ice motion products (Meier and Dai 2006).

The 89-GHz channel has a limitation: Compared to lower-frequency channels, it is more highly sensitive to atmospheric moisture, which increases spurious vector estimates. Specifically, cloud contamination on images of brightness temperature (Tb) distorts local Tb fields and results in false peaks in a cross-correlation plane. During the last two decades, the risk of a decreased retrieval performance due to such contamination could have increased even during cold and dry winters, due to the increasing influxes of cyclones from the midlatitudes to the Arctic Ocean resulting from sea ice losses in the preceding summer (Valkonen et al. 2021). The Tb fields are also distorted by surface melting or increased sea ice mobility, regardless of the PMW frequency, which makes retrievals difficult in the summer, despite the growing demands for SIMV products to assist in forecasting the accessibility of the Northern Sea Route. Such issues highlight the increasing importance of validating vector fields derived by correlation-based tracking.

In general, the basic processing steps used to retrieve SIMVs are as follows: First, raw vector fields are obtained based on the MCC method. Second, the raw data are validated by comparing them with neighboring vectors to filter questionable vectors as outliers. Additional filtering is often conducted by a comparison with reanalysis local wind vectors (Kwok et al. 1998; Kwok 2008), based on the empirical relationship between sea ice and wind vectors first indicated by Nansen (1902) and then followed in subsequent studies (e.g., Thorndike and Colony 1982). Third, the resultant missing data are complemented by merging multiple data sources (e.g., Girard-Ardhuin and Ezraty 2012) or by temporal or spatial interpolation (e.g., Kimura et al. 2013). In this sequential processing, the validation of vector fields depends on the second step; however, neighborhood-based filtering reduces its efficiency when a search area is extensively under weather or surface melting effects. Validation with wind data also becomes less effective when the old rule of thumb of the sea ice response to wind forcing is inapplicable to sea ice motions anomalously amplified by increased sea ice mobility with changes in their properties (Spreen et al. 2011; Kwok et al. 2013). Besides the wind forcing, underlying ocean currents especially in coastal regions, as well as internal ice stress gradients of the compact pack ice, affect sea ice motions. Furthermore, because outlier vectors are associated with maximum (i.e., first) cross-correlation peaks in the contaminated cases, signals of valid vectors are obscured, and they are in turn associated with second or third peaks; they are thus undetectable in the MCC scheme. Therefore, it is beneficial to introduce a novel validation approach that selects optimal vectors from multiple candidates nominated by cross-correlation peaks including false peaks.

Outside geophysical motion tracking using satellite observations, a validation method for motion fields estimated by image processing has been established using laboratory flow visualization techniques, such as particle image velocimetry (PIV) (Raffel et al. 2018). Along with neighborhood-based validation, PIV commonly validates raw vector fields by referring to essential flow information derived from fluid dynamics or additional simultaneous observations: for example, the stereo-PIV technique. This validation procedure screens out invalid vectors and replaces them with reference data to fill gaps in the motion fields.

In this study, we applied this validation method to select optimal vectors from multiple candidates. As reference data, we employed large-scale sea ice displacement extracted using lower-frequency data, with the aim of obtaining the reference motion field via simultaneous observations that contained fewer weather effects. We then selected the vector closest to the reference vector for each grid, which was the optimal local solution. This selection procedure simultaneously identified areas where 89-GHz data were unavailable for retrieving SIMVs when all candidates were not tolerated as valid vectors. In such areas, we adopted retrievals from lower-frequency images based on the perspective of providing reliable SIMV fields using only AMSR2 (which is a single sensor but has multiple channels with fine resolutions). The channels used here are summarized in Table 1, along with their footprint resolutions.

In addition to validation using the retrieval algorithm, it is useful to conduct an uncertainty assessment to evaluate satellite-derived products by comparing them with in situ data. Currently, buoy observations, which provide sea ice velocities along their GPS trajectories, have been utilized to conduct assessments. Most of their observations are limited to multiyear ice floes; however, the Arctic sea ice thickness has substantially decreased with large replacements of multiyear ice by first-year ice in not only the marginal seas but also in the basin areas (Maslanik et al. 2011; Laxon et al. 2013). Additionally, Sumata et al. (2014, 2015) showed that uncertainty increases with a decrease in sea ice thickness through intercomparisons between several products, suggesting the need for assessing uncertainties in first-year ice areas. Therefore, we utilized acoustic measurements of sea ice velocities from fixed-site ocean moorings that captured both multiyear and first-year ice. In this study, we assessed retrieved SIMVs from a methodological perspective based on the winter

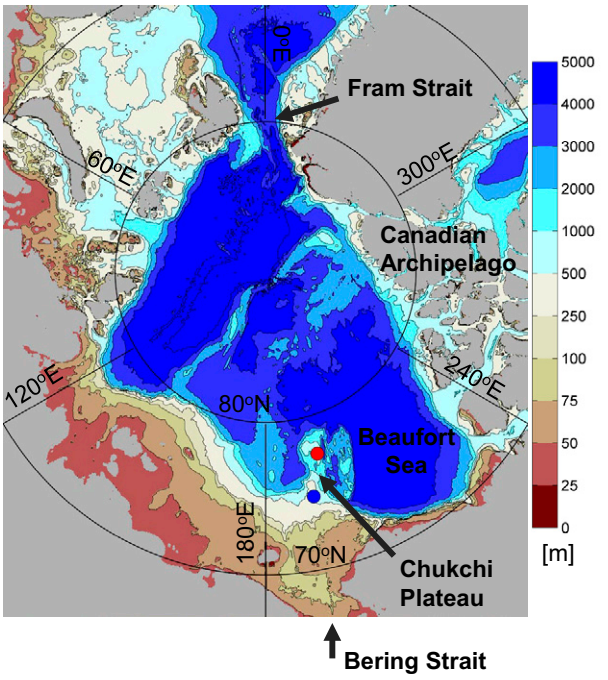

FIG. 1. Map of study area. Seafloor bathymetries from the IBCAO, version 4.0 (Jakobsson et al. 2020), are shown using different colors. The locations of ocean moorings carrying ADCPs to measure in situ sea ice velocities are indicated by the red and blue dots. The specific mooring locations are listed in Table 2.

comparison with in situ data and discussed the applicability of our algorithm to the summer retrieval that is still challenging due to the presence of the aforementioned error sources.

The objective of this study, therefore, was to demonstrate the performance of an algorithm that selects optimal vectors based on the validation with reference data using AMSR2 multichannel data from the Arctic Ocean [Fig. 1 with bathymetries from the International Bathymetric Chart of the Arctic Ocean (IBCAO) version 4.0 from Jakobsson et al. (2020)], with a particular focus on the availability of 89-GHz data. Here, we describe the characteristics of the validated vectors through year-round retrievals and assess the uncertainty of the retrieved SIMVs using in situ data. It is acknowledged that Tschudi et al. (2010, 2020) developed an alternative approach for reducing impacts of questionable vectors by interpolating data sources other than PMW observations. In addition, Lavergne et al. (2021) recently presented another approach for enhancing retrievals by swath-to-swath motion tracking. However, making comparisons between the results of these studies and ours is currently beyond the scope of this study.

The remainder of this paper is organized as follows. Section 2 is a data description, section 3 describes the proposed algorithm, section 4 presents the features of the vector fields derived using the optimal selection algorithm and the results of the uncertainty assessment, and the conclusions are presented in section 5.

2. Data

a. Data for retrievals

We accessed the *GCOM-W* AMSR2 level-1R (L1R) product of calibrated Tb data in swath projections, version 2, provided by the Japan Aerospace Exploration Agency (JAXA). The retrieval period was from 2013 to 2020. To take advantage of the high-resolution 89-GHz channel data in motion tracking, we created daily Tb images for each horizontal and vertical polarization on a 5-km polar stereographic projection using orbit data with a native footprint resolution from the L1R product. The daily averaged images of Tb (and its observational time used to convert displacements to vectors) were composed of orbit data observed from 0000 to 2359 UT. This was conducted by interpolating each orbit data to the polar stereographic projection using Delaunay triangulation, and in turn by averaging the interpolated data at each pixel. For one winter season from October 2014 to April 2015, we retrieved three types of SIMVs by trial using images generated from 1) descending, 2) ascending, and 3) both orbit data, respectively. As uncertainties of each retrieved result relative to in situ data (see its description in section 2b) showed no significant difference [less than 1 mm s^{-1} differences in root-mean-square errors (RMSEs)], we used only descending orbit data to create daily images for reducing computational loads. Daily images of 19- and 37-GHz-channel data were created in the same manner. Additionally, the images were oversampled (see details in section 3a).

AMSR2 level-3 (L3) sea ice concentration product, version 3, was also used to determine the sea ice pixels where SIMV retrievals were processed. Sea ice pixels were those in which the sea ice concentration values were greater than 15%. The L3 product mapped onto a 10-km polar stereographic projection was linearly interpolated to a 5-km resolution for joint use with Tb images.

To identify outliers in the retrieved SIMV fields based on the relationship between sea ice drift and wind forcing, daily averaged surface wind data were generated using 6-hourly surface wind data obtained from the National Centers for Environmental Prediction–National Center for Atmospheric Research (NCEP–NCAR) reanalysis dataset provided by 2.5° × 2.5° global grids (Kalnay et al. 1996). The reanalysis wind data were interpolated to the polar stereographic projection with a 50-km resolution using Delaunay triangulation.

b. In situ data for uncertainty assessment

To assess the uncertainty in the retrieved SIMVs, we used in situ sea ice velocity data measured using upward-looking acoustic Doppler current profilers (ADCPs; Workhorse sentinel 600 kHz) mounted on two ocean moorings deployed in the northern and southern Chukchi Plateau (hereinafter referred to as NCP and SCP), respectively. Table 2 summarizes the specific locations and durations of the measurements. The ADCPs measured the velocities using a bottom tracking mode that estimated the velocities by ranging the distance to the sea ice bottom when the tilt of a mooring array was in the

TABLE 2. Locations and durations of moored ADCP measurements. The locations of the NCP and SCP moorings are denoted in Fig. 1 by red and blue dots, respectively.

Area	Lat (°N)	Lon (°E)	Duration	Sampling interval (min.)
Northern Chukchi Plateau (NCP)	77.47	195.88	August 2013–August 2015	20
Southern Chukchi Plateau (SCP)	74.80	192.10	August 2014–August 2015	45

range of ±15°. Errors in the velocities due to magnetic declinations were corrected. To compare with satellite products, daily averaged velocities were calculated using these corrected data samples obtained within ±12 h relative to the mean observational time of retrieved SIMVs at the four grids that were closest to each mooring site. The precision of the daily velocities was dictated by the measurement setting and ensemble averaging and was estimated to be ±0.20 and ±0.53 mm s^{-1} for the NCP and SCP moorings, respectively. This precision is high enough to evaluate the performance of satellite retrievals but is well known to significantly decrease in marginal ice zones with low sea ice concentrations because acoustic bottom tracking measurements are violated by contaminations of signals from ice-free sea surfaces (Melling et al. 1995). To avoid using such less accurate in situ data for the assessment, we adopted in situ data measured only when the mooring sites were in fully ice-covered conditions (identified by AMSR2 sea ice concentration values greater than 95%).

As previously stated in section 1, the main reason for employing these limited measurements was to assess the retrieved results under a variety of sea ice conditions. As these moorings experienced seasonal sea ice retreats and recoveries, and they were located on the pathway of multiyear ice floes delivered by the Beaufort Gyre, they provided data records under the mixed conditions of first-year ice and multiyear ice during winter (the detailed conditions are provided in section 4b).

3. Algorithm

a. *Estimating vector candidates by detecting multiple cross-correlation peaks*

In this study, sea ice displacements were estimated by the following two steps using 5-km Tb images of 89 GHz. First, the forward position of an $n \times n$ pixel window centered around a target position was searched in an $m \times m$ pixel area in the subsequent imagery by computing spatial lag correlations by shifting the pixel window. We set $n = 10$ and $m = 50$ so that the pixel window and search area sizes were 50 and 250 km, respectively. Second, once a pair of pixel windows exhibiting a maximum cross-correlation peak was detected, these windows were linearly oversampled by a factor of 3 to estimate displacements at subpixel level, and the maximum cross-correlation peak of an $n \times n$ pixel window was detected again using the oversampled image pixels. In the second step, a search area was predefined by peak searching in the first step, to shorten the computational load for retrieval. Finally, the displacement information estimated by detecting cross-correlation peaks was converted to vector components using the differences in the observational time between the two successive images. As the maximum cross-correlation peak is not always caused by actual sea ice displacements, individual motion fields detected by the N highest cross-correlation peaks were prepared as candidates for valid vectors. In this study, $N = 3$ was used.

In terms of reducing quantization noise, slower motion detectability is key to improving performances of correlation-based tracking of sea ice motion. Therefore, a minimum vector component to be detected in each x and y direction, which is estimated by an image pixel length and temporal interval of tracking, was utilized as a motion precision in theory (e.g., Tschudi et al. 2020). In our algorithm for daily motion tracking, the precision of 89-GHz vectors was estimated to be 5 km day^{-1} (i.e., 5.8 cm s^{-1}) using the pixel length of 5 km and was further improved to 1.67 km day^{-1} (i.e., 1.9 cm s^{-1}) by the subpixel level tracking using the 3-times oversampled images. Here, we focus on the 89-GHz vectors but a precision of 19- and 37-GHz vectors further decreased due to their coarser footprint resolutions.

As mentioned in section 1, the accuracy of motion tracking is decreased by diurnal Tb changes due to cloud contamination or the summer melting of the ice cover. The differences between averaged Tb values in paired pixel windows are usually employed to identify false matches in cross-correlation peak detection (Kwok et al. 1998). However, this procedure was not used here because the outlier vectors rarely overlapped areas that had large Tb differences in the retrievals during 2013–20.

In addition to such seasonal effects, accuracy decreases regionally near ice edges when sea ice drains into open water areas, or when it fragments during collisions with coastal boundaries. To avoid these situations, peak detection was not conducted when the entire target pixel window was not filled by sea ice pixels, and extrapolated values were obtained using neighboring vectors. These extrapolated values were not used for uncertainty assessments.

By iterating the above process, individual vector fields were prepared from images of 89-, 37-, and 19-GHz horizontal and vertical polarizations at daily intervals. Furthermore, to increase the accuracy of the large-scale displacements that were used as reference data, fields computed by cross-correlation peak detection using larger pixel windows (100 and 150 km) were also prepared.

b. *Deriving reference vector field*

To derive the reference vector fields, vectors from 19- and 37-GHz images were used as inputs, regardless of the polarization and pixel window size used for motion tracking. These vectors were removed from the inputs if they did not satisfy the conditions configured by using the following: 1) acceptable cross correlations, 2) the relationship between vector candidates and reanalysis local surface winds, and 3) the relationship between vector candidates and the preferential displacement

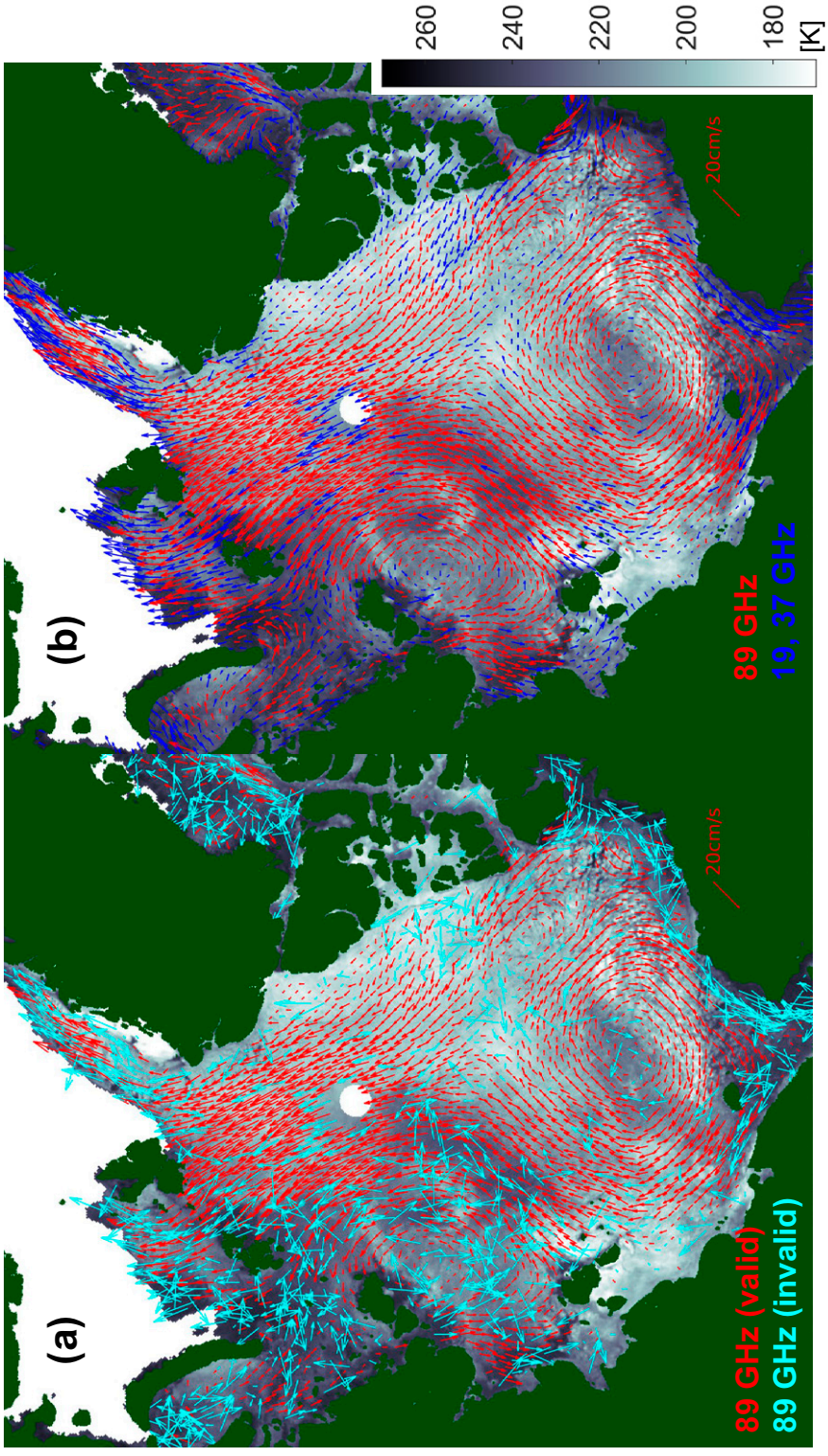

FIG. 2. Retrieved SIMV fields by (a) the MCC method using 89-GHz data and (b) the optimal selection algorithm using multichannel data on 26 Dec 2014, plotted on Tb images observed using the vertically polarized 89-GHz channel. In (a), vectors judged as valid and invalid in our algorithm are red and cyan colored, respectively; the arrow scaling factor to plot vectors is fixed when vector magnitudes are greater than 20 cm s^{-1}. In (b), vectors from 89-GHz data and those from 19- to 37-GHz data are red and blue colored, respectively.

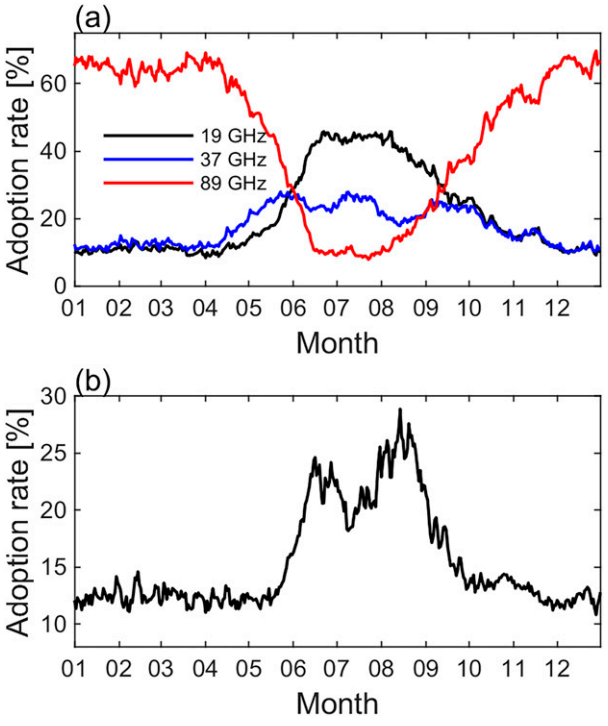

FIG. 3. Seasonal variations in an adoption rate of (a) vectors selected as optimal ones from individual motion fields from 89-, 37-, and 19-GHz images (red, blue, and black lines, respectively), and (b) reference vectors in 2013–20. The values are averaged in the study area, with the exception of those in the areas south of the Fram and Bering Straits and the Canadian Archipelago.

information estimated by conducting a velocity probability density function analysis.

For the first condition, low cross correlations did not necessarily indicate invalid vectors; nonetheless, vectors were not accepted if their cross correlations are below 0.3. More than 90% of candidates were accepted in October–May, but acceptable candidates dropped to approximately 70% in June–September. This suggested that Tb fields within pixel windows were distorted by weather or surface melting effects as well as increased sea ice mobility during summer.

For the second condition, vector candidates were rejected if they were not within $\pm 60°$ of the reanalysis surface wind vectors, which is the same threshold as that used in previous studies (e.g., Kwok et al. 1998). This is not tight thresholding, because less than 10% of the candidates throughout the year were rejected.

The third condition was set using a mode vector derived from a probability density function analysis using vectors in 3×3 grids centered on the target position. All the surrounding candidates satisfying the first two conditions were used in this calculation. Based on a vector difference test that calculated a magnitude of a vector difference between candidate and mode vectors, candidates were rejected if the magnitudes were above the empirical criterion that was set to 30 cm s^{-1} in this study. After a sequence of filtering processes, several vector candidates were maintained in each grid. The reference vector field was given by a spatially averaged field using a mean filter with these maintained vectors.

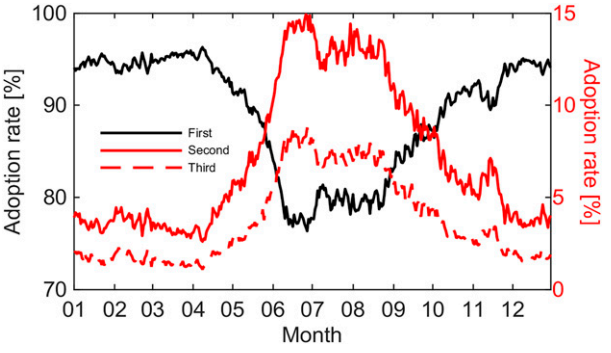

FIG. 4. Seasonal variations in the adoption rate of optimal vectors detected by first, second, and third peaks in 2013–20 (black solid, red solid, and red dashed lines, respectively). The values are averaged in the study area, with the exception of those in the areas south of the Fram and Bering Straits and the Canadian Archipelago.

c. *Selecting optimal vectors using reference field*

Finally, an optimal vector was selected at each processing grid from the candidates prepared using 89-GHz images as presented in section 3a. The selection was based on the vector difference test between the candidate and reference vectors: The candidate exhibiting the smallest vector difference was chosen as the optimal solution regardless of N and satellite channel polarizations. The algorithm empirically determines that vectors are rejected as invalid when the magnitudes of the differences are above 10 cm s^{-1}. In turn, data gaps in vector fields, which were caused by the rejection of all 89-GHz vector candidates, were filled by the following two steps. First, an optimal vector was searched again by the above selection procedure using candidates from individual vector fields estimated using 19- and 37-GHz images without prioritizations between the two frequencies. Second, if these lower-frequency vector candidates did not pass the selection, the reference vector was inserted. This successive selection procedure enabled vector fields to be obtained without the use of spatial interpolation or correction by surrounding neighbors, except for the grids where the reference vectors were inserted. The following section presents the features of the selected vectors, using year-round retrieval.

4. Results and discussion

a. *Features of optimal vector fields*

To qualitatively analyze the optimal selection performance, Fig. 2 compares snapshots of vector fields plotted on vertically polarized 89-GHz Tb images on 26 December 2014, which was detected using the MCC method and our algorithm. Figure 2a shows that outlier vectors linked to maximum cross-correlation peaks calculated using 89-GHz data emerge even in winter (cyan-colored vectors); particularly, they are clustered over the eastern Arctic. In vector fields from 19- and 37-GHz data using the MCC method, the outliers are decreased compared with that from 89-GHz data; however, they are not negligible over the same areas (not shown), which suggests that both 89-GHz and lower-frequency data suffer

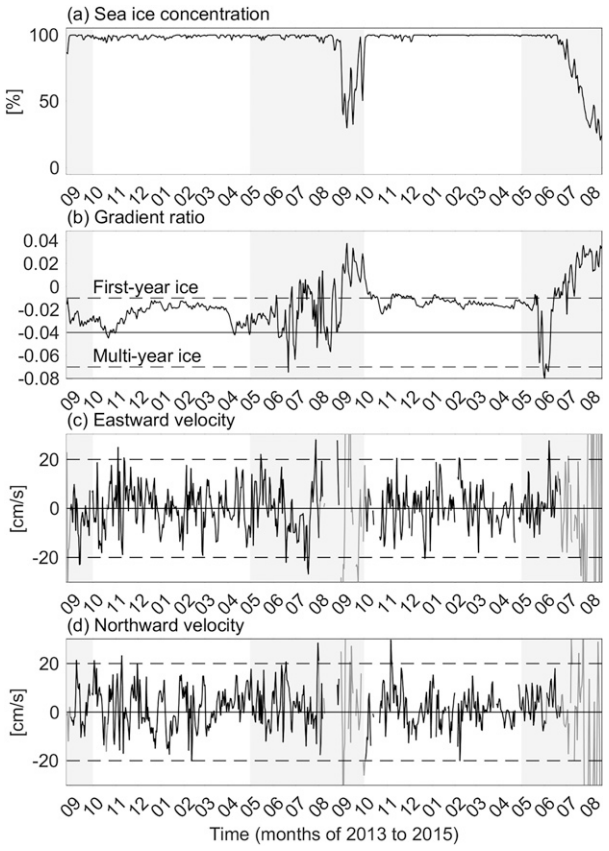

FIG. 5. Time series of (a) sea ice concentration, (b) gradient ratio calculated using 19- and 37-GHz Tb for vertical polarization, (c) in situ eastward sea ice velocity, and (d) in situ northward sea ice velocity, at the NCP mooring site. Durations without (with) gray shading indicate winter (summer) months [October–April (May–September)]. In (a) and (b), the values are given using the spatially weighted averages of data within ±25 km of the mooring site; in (b) the dashed lines at the two tie points identify multiyear and first-year ice, and the solid line indicates their intermediate value; in (c) and (d), daily averaged velocities, whose precision is guaranteed (unguaranteed) due to ice-congested (-uncongested) conditions, are shown by black (gray) lines.

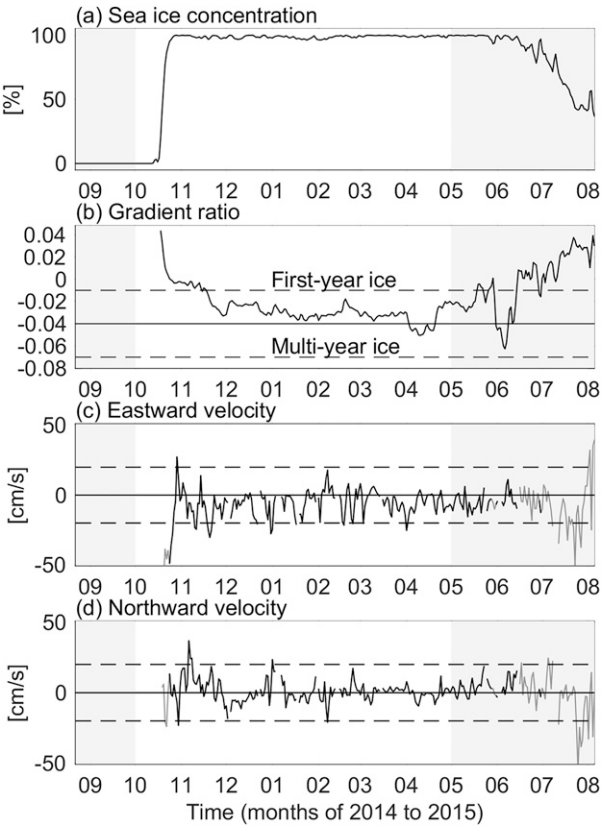

FIG. 6. As in Fig. 5, but for the SCP mooring site.

from weather effects. Figure 2b shows that the visible outliers present in Fig. 2a were successfully replaced by valid vectors detected by the second or third cross-correlation peaks, owing to validation with the reference data. The resultant vector fields mostly comprise 89-GHz data.

To show the seasonal availability of data at each frequency for retrievals, Fig. 3a shows the seasonal variations in the adoption rate of vectors from the individual motion fields. In the figure, the polarization of each channel is not discriminated. In November–April, vectors from 89-GHz data account for approximately 60% of the Arctic motion field, while those from 37- and 19-GHz data account for approximately 10% each. This indicates that the 89-GHz data are available to retrieve the Arctic motion field in winter months; however, validation with lower-frequency data is essential to avoid questionable vectors that occur intermittently and are likely due to weather effects.

However, the availability of 89-GHz data begins to decrease in May, and it composes only 10% of the motion field in June–July when lower-frequency data (especially 19-GHz data) are responsible for retrievals instead (Fig. 3a). This selectivity of the PMW frequency conforms with the results shown by Kwok (2008), who utilized 19-GHz data to improve summertime retrievals. However, the availability of these lower-frequency data remains at approximately 40% and 20% for 19 and 37 GHz, respectively, from June to July and thus reference data given by spatial averages are inserted to fill data gaps in vector fields (Fig. 3b). These results indicate a difficulty of obtaining daily vector fields without spatial or temporal interpolations in these months because the retrieval based on PMW image processing is hampered by certain error sources, as described in section 1. This emphasizes the importance of providing data quality information based on the validation process, particularly for summer products.

Figure 4 also shows the seasonal variations in the adoption rate of the selected vectors detected by the first, second, and third cross-correlation peaks. In the figure, the frequency and polarization corresponding to the selected vectors are not discriminated. The selected vectors associated with the first cross correlations comprises more than 90% of the motion field in October–April, but this rate decreases to approximately 80% in June–August. In contrast, the rate of vectors associated with the second and third cross correlations increases during the summer months. This result also confirms that the validation step

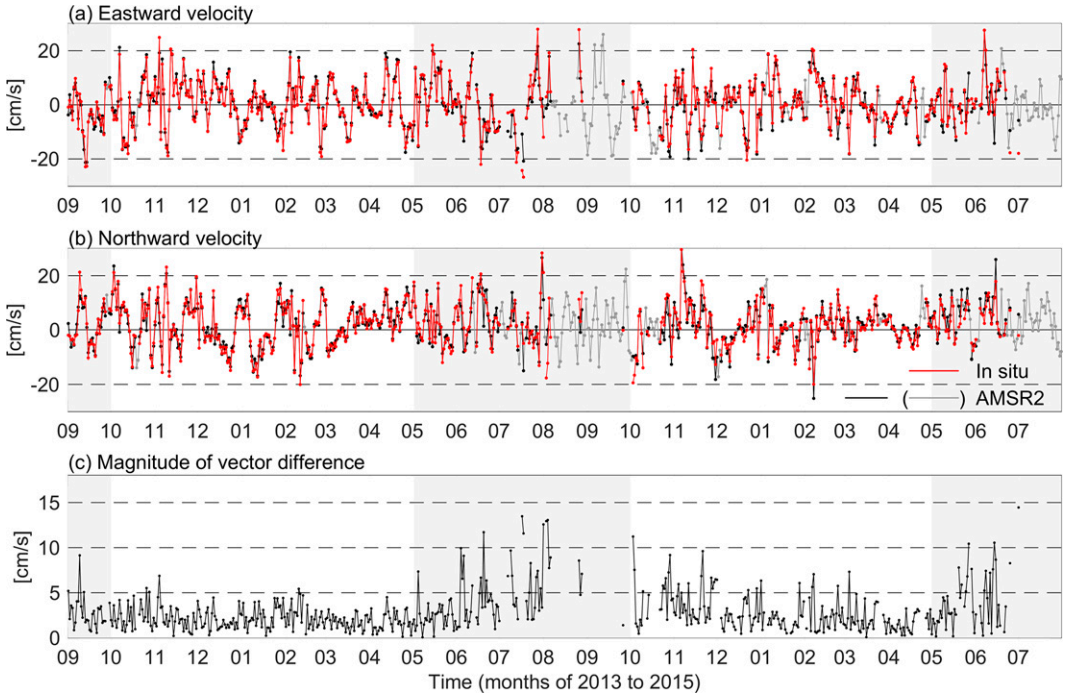

FIG. 7. Time series of (a) eastward and (b) northward sea ice velocities from the NCP mooring (red lines), and those that were retrieved using AMSR2 data (black and gray lines), and (c) magnitudes of vector differences between in situ and retrieved vectors. Durations without (with) gray shading indicate winter (summer) months [October–April (May–September)]. In (a) and (b), retrieved velocities are plotted by black (gray) lines when the high precision in situ data were available (unavailable) for uncertainty assessments.

extends the applicability of correlation-based motion tracking by searching for valid vectors from candidates linked to low-order cross-correlation peaks.

b. *Uncertainty assessments based on comparisons with in situ data*

Before we compare the AMSR2 SIMV with in situ data, we describe the sea ice conditions at the mooring locations, as these are critical to the in situ data quality, as well as the applicability of correlation-based motion tracking. At the locations of both the NCP and SCP moorings, sea ice concentrations exhibited seasonal increasing (decreasing) trends in the winter (summer) (Figs. 5a, 6a). Here, winter months are from October to April, in which the concentrations were approximately 100%, and summer months are from May to September. Together with the sea ice concentration, Figs. 5b and 6b show time series of the gradient ratio introduced to distinguish multiyear ice from first-year ice using their emissivity changes with PMW frequency (Cavalieri et al. 1984). The ratio was calculated using the Tb data of the vertically polarized 19- and 37-GHz channels. Its smaller (larger) ratios were associated with multiyear (first-year) ice. In the figures, the dashed lines represent the values at the two tie points configured to identify multiyear and first-year ice in the NASA team sea ice concentration algorithm applied to the AMSR-E data (Markus and Cavalieri 2009), and the solid lines represent their intermediate values. During most of the two winter seasons, the ratio was above the intermediate value at the NCP mooring site (Fig. 5b), which indicated that first-year ice predominated. On the other hand, the ratio fluctuated around the intermediate value at the SCP mooring site (Fig. 6b), which indicated that multiyear ice was mixed with first-year ice around the site. Using these in situ data, satellite retrievals were assessed in not only multiyear ice conditions but also in those of first-year ice.

Figures 5c, 5d, 6c, and 6d show time series of daily in situ sea ice velocities, in which black (gray) lines display the in situ data with the high precision guaranteed (unguaranteed) due to ice-congested (-uncongested) conditions. During the winter months, most data were collected with sufficient precision to be used for assessing satellite retrieval. Although they became unreliable as the summer progressed, the high precision was also assured even in the summer months partly (e.g., September 2013, May–July 2014, and May–June 2015 at the NCP mooring). The averaged magnitudes of eastward and northward velocities employed for the assessment were 6.7 ± 5.6 (8.0 ± 7.4) and 6.4 ± 5.0 (5.6 ± 5.5) cm s^{-1} for the NCP (SCP) mooring. As these typical velocity magnitudes in the basin area are comparable to a minimum magnitude to be detected using 89-GHz data with a native footprint resolution, a subpixel level tracking based on an oversampling technique of Tb images was expected to contribute to improving retrieval performances.

We then assessed the AMSR2 SIMVs by comparing with in situ data obtained in the winter months, when correlation-based motion tracking is robust because of the compactness or surface unambiguity of the ice cover. The winter

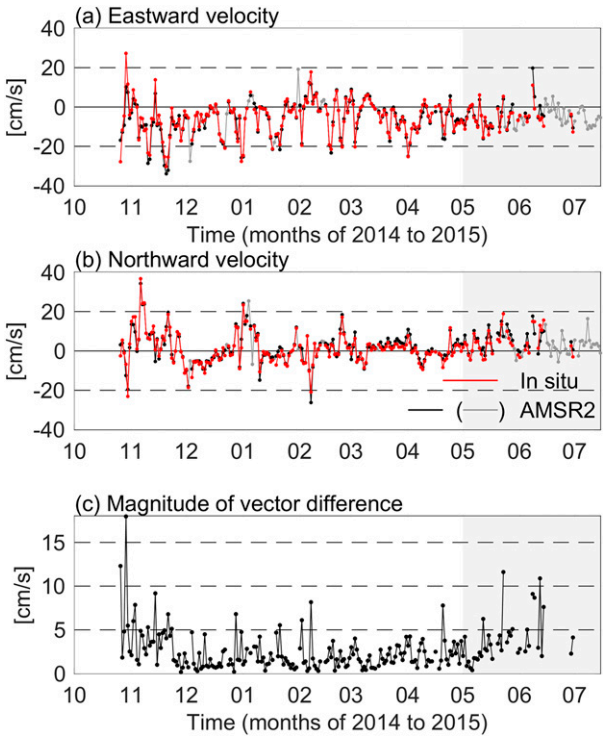

FIG. 8. As in Fig. 7, but for the SCP mooring site.

comparisons are shown in areas without gray shadings in Figs. 7 and 8. The retrieved vectors showed good agreement with the in situ data in both direction and magnitude at the two mooring sites (Figs. 7a,b, 8a,b), despite the mixed conditions of multiyear and first-year ice (Figs. 5b, 6b). This is also confirmed by the time series of magnitudes of vector differences between in situ and retrieved vectors (Figs. 7c, 8c); specifically, the magnitudes were below 5 cm s^{-1} in most of the winters even though occasional increases appeared. Table 3 summarizes the statistics calculated using these time series data. The RMSEs were 1.0 (2.5) cm s^{-1} in the eastward components and 1.6 (1.8) cm s^{-1} in the northward components at the NCP (SCP) mooring location.

We subsequently focused on comparing results in the summer months when the robustness of motion tracking tends to decrease. The summer comparisons are shown in areas with gray shadings in Figs. 7 and 8. Although it seems that the actual sea ice motions were well tracked even in summers (Figs. 7a,b, 8a,b), differences between in situ and retrieved vectors tend to be amplified compared to those in winters (Figs. 7c, 8c). The amplified differences remind us of the two causes of satellite product degradation: one relates to the methodological limitation that results in the similarity of image pixel templates becoming undetectable when there are large diurnal Tb changes. As described in section 3a, larger diurnal Tb changes are not necessarily related to outlier vectors, and hence, separating its relative impact on the decreased retrieval performance is not straightforward. The other is dictated by the spatial resolution of Tb images: The motion precision decreases when the lower-frequency Tb images are used for retrievals instead of the high-resolution 89-GHz images. Specifically, more than 80% of vectors were retrieved from 89-GHz data in winter for the two mooring sites but only 33% and 15% in summer for the NCP and SCP moorings, respectively. This supports the idea that the decreased motion precision is one of the possible causes of the increased uncertainty.

TABLE 3. Statistics obtained from comparing AMSR2 SIMV with in situ data measured by moored ADCPs mounted on the NCP and SCP ocean moorings in winter months (October–April). The RMSE and bias are in cm s^{-1}.

		Eastward velocity			Northward velocity		
Mooring	*N*	RMSE	Bias	*R*	RMSE	Bias	*R*
NCP	396	1.0	−0.12	0.98	1.6	−0.13	0.97
SCP	180	2.5	−0.50	0.96	1.8	0.47	0.95

While the assessment of the retrieved results in this study was limited to a case of high sea ice concentration in terms of quality control of in situ data, the satellite retrieval is capable of providing vector estimates even in a case of low sea ice concentration as shown by gray lines in Figs. 7a, 7b, 8a, and 8b. However, actual sea ice motion exhibits high temporal variability in the latter case rather than that in the former case; for example, an inertial sea ice oscillation with about a subdaily cycle is amplified (damped) with increased (decreased) sea ice mobility associated with decreased (increased) sea ice concentration (Gimbert et al. 2012). According to the Nyquist theorem, such a subdaily cycle component is unable to be resolved by the daily motion tracking using satellite images and thus is expected to appear as noise, especially in summer retrievals. Furthermore, the retrieval involves the additional complication of high spatial variability of motion fields resulting from the drift ice rheology changing drastically with increased ice deformation (e.g., Leppäranta 2011). To develop proper techniques to monitor such high spatiotemporal variability beyond the satellite capability in terms of the resolution, as well as their assessment methods based on in situ measurements, further investigations are needed in the combination of satellite monitoring with additional approaches such as data assimilation.

5. Conclusions

We propose an algorithm that uses a high-resolution AMSR2 89-GHz channel and which can be used to provide reliable daily SIMVs. Using this channel has the potential to enhance the theoretical motion precision, and it also increases the number of erroneous motion estimates owing to its higher sensitivity to atmospheric moisture compared to lower-frequency channels. To avoid such erroneous estimates, we introduce a validation step that uses motion fields retrieved from 19- and 37-GHz data to determine whether each vector candidate is valid when multiple candidates are detected by the *N* highest cross-correlation peaks. The main advantages of validation using reference data are twofold: First, vector fields retrieved from 89-GHz images are validated via simultaneous multichannel

observations by the AMSR2 sensor. Second, data gaps in vector fields in most winter cases can be filled without spatial interpolations by neighboring vectors because outlier vectors linked to the first cross-correlation peaks are replaced by candidates detected by low-order cross-correlation peaks or candidates from lower-frequency images (as long as the validation tolerates them as valid vectors based on the vector difference test). With this advantage, more 89-GHz data are available in winter motion field retrievals. The uncertainty assessment using in situ data demonstrates that the retrieved vectors correlate well with observational evidence, and that RMSEs between satellite and in situ data were only 1–2 cm s^{-1}, even at a daily temporal resolution in winter.

However, the results show that 89-GHz data are inapplicable for use in summer retrievals, mainly due to weather effects; therefore, vector fields tend to consist of candidates from 19- and 37-GHz data. However, the validation process determines that vector candidates are not tolerated as valid for up to 25% of the summer motion fields, regardless of the PMW frequency. This means that motion tracking based on PMW image processing is significantly hampered by local distortions of Tb images, owing to sea ice melt or advection, which is inevitable even with the use of multichannel data. Nevertheless, the validation process presented here is useful for shaping the applicability limit of PMW-based SIMV retrieval, and it serves as a bridge for the further development of SIMV data using alternative approaches.

Validation with reference data provides winter vector fields without spatial interpolations by neighboring vectors, so that the discontinuity of sea ice motion fields originating from the solid nature of the ice cover is maintained. Around discontinuous velocity fields, sea ice divergence/convergence is reinforced, and this plays an important role in the heat and momentum balances in polar climate systems. For instance, divergent motions cause winter ice opening, which results in increased air–ocean heat exchanges (Maykut 1978), and convergent motions lead to mechanical ice thickening, which is an important precondition for summer sea ice recovery (Park et al. 2018). Our products will be useful for evaluating the dynamic impacts underestimated by spatially smoothed vectors.

Acknowledgments. This work was supported by the JAXA research projects [IARC-JAXA Information System and First Research Announcement on the Earth Observations (EO-RA1)] and the Green Network of Excellence (GRENE) Program. We are grateful to the captains, officers, and crews of the *Araon* for their efforts in the deployment and recovery of ocean moorings, and to the anonymous reviewers for their helpful comments.

Data availability statement. The AMSR2 brightness temperature and sea ice concentration data were downloaded from https://gportal.jaxa.jp. Their version information is provided at https://suzaku.eorc.jaxa.jp/GCOM_W/data/w_productinfo.html. The NCEP/NCAR reanalysis dataset is available at https://psl.noaa.gov/data/gridded/data.ncep.reanalysis.html. The in situ data utilized in this study can be accessed by contacting Tokyo University of Marine Science and Technology (email: koji@kaiyodai.ac.jp).

REFERENCES

Agnew, T. A., L. E. Hao, and T. Hirose, 1997: Estimation of large-scale sea-ice motion from SSM/I 85.5 GHz imagery. *Ann. Glaciol.*, **25**, 305–311, https://doi.org/10.3189/S0260305500014191.

Cavalieri, D. J., P. Gloersen, and W. J. Campbell, 1984: Determination of sea ice parameters with the Nimbus 7 SMMR. *J. Geophys. Res.*, **89**, 5355–5369, https://doi.org/10.1029/JD089iD04p05355.

Emery, W. J., A. C. Thomas, M. J. Collins, W. R. Crawford, and D. L. Mackas, 1986: An objective method for computing advective surface velocities from sequential infrared satellite images. *J. Geophys. Res.*, **91**, 12 865–12 878, https://doi.org/10.1029/JC091iC11p12865.

——, C. W. Fowler, J. Hawkins, and R. H. Preller, 1991: Fram Strait satellite image-derived ice motions. *J. Geophys. Res.*, **96**, 4751–4768, https://doi.org/10.1029/90JC02273.

Gimbert, F., D. Marsan, J. Weiss, N. C. Jourdain, and B. Barnier, 2012: Sea ice inertial oscillations in the Arctic basin. *Cryosphere*, **6**, 1187–1201, https://doi.org/10.5194/tc-6-1187-2012.

Girard-Ardhuin, F., and R. Ezraty, 2012: Enhanced arctic sea ice drift estimation merging radiometer and scatterometer data. *IEEE Trans. Geosci. Remote Sens.*, **50**, 2639–2648, https://doi.org/10.1109/TGRS.2012.2184124.

Jakobsson, M., and Coauthors, 2020: The International Bathymetric Chart of the Arctic Ocean version 4.0. *Sci. Data*, **7**, 176, https://doi.org/10.1038/s41597-020-0520-9.

Kalnay, E., and Coauthors, 1996: The NCEP/NCAR 40-Year Reanalysis Project. *Bull. Amer. Meteor. Soc.*, **77**, 437–472, https://doi.org/10.1175/1520-0477(1996)077<0437:TNYRP>2.0.CO;2.

Kimura, N., A. Nishimura, Y. Tanaka, and H. Yamaguchi, 2013: Influence of winter sea-ice motion on summer ice cover in the Arctic. *Polar Res.*, **32**, 20193, https://doi.org/10.3402/polar.v32i0.20193.

Kwok, R., 2008: Summer sea ice motion from the 18 GHz channel of AMSR-E and the exchange of sea ice between the Pacific and Atlantic sectors. *Geophys. Res. Lett.*, **35**, L03504, https://doi.org/10.1029/2007GL032692.

——, A. Schweiger, D. A. Rothrock, S. Pang, and C. Kottmeier, 1998: Sea ice motion from satellite passive microwave imagery assessed with ERS SAR and buoy motions. *J. Geophys. Res.*, **103**, 8191–8214, https://doi.org/10.1029/97JC03334.

——, G. Spreen, and S. Pang, 2013: Arctic sea ice circulation and drift speed: Decadal trends and ocean currents. *J. Geophys. Res. Oceans*, **118**, 2408–2425, https://doi.org/10.1002/jgrc.20191.

Lavergne, T., S. Eastwood, Z. Teffah, H. Schyberg, and L. A. Breivik, 2010: Sea ice motion from low-resolution satellite sensors: An alternative method and its validation in the Arctic. *J. Geophys. Res.*, **115**, C10032, https://doi.org/10.1029/2009JC005958.

——, M. Piñol Solé, E. Down, and C. Donlon, 2021: Towards a swath-to-swath sea-ice drift product for the Copernicus Imaging Microwave Radiometer mission. *Cryosphere*, **15**, 3681–3698, https://doi.org/10.5194/tc-15-3681-2021.

Laxon, S. W., and Coauthors, 2013: CryoSat-2 estimates of Arctic sea ice thickness and volume. *Geophys. Res. Lett.*, **40**, 732–737, https://doi.org/10.1002/grl.50193.

Leppäranta, M., 2011: *The Drift of Sea Ice*. 2nd ed. Springer, 350 pp., https://doi.org/10.1007/978-3-642-04683-4.

Liu, A. K., Y. Zhao, and S. Y. Wu, 1999: Arctic sea ice drift from wavelet analysis of NSCAT and special sensor microwave imager data. *J. Geophys. Res.*, **104**, 11 529–11 538, https://doi.org/10.1029/1998JC900115.

Markus, T., and D. J. Cavalieri, 2009: The AMSR-E NT2 sea ice concentration algorithm: Its basis and implementation. *J. Remote Sens. Soc. Japan*, **29**, 216–225, https://doi.org/10.11440/rssj.29.216.

Maslanik, J., J. Stroeve, C. Fowler, and W. Emery, 2011: Distribution and trends in Arctic sea ice age through spring 2011. *Geophys. Res. Lett.*, **38**, L13502, https://doi.org/10.1029/2011GL047735.

Maykut, G. A., 1978: Energy exchange over young sea ice in the central Arctic. *J. Geophys. Res.*, **83**, 3646–3658, https://doi.org/10.1029/JC083iC07p03646.

Meier, W. N., and M. Dai, 2006: High-resolution sea-ice motions from AMSR-E imagery. *Ann. Glaciol.*, **44**, 352–356, https://doi.org/10.3189/172756406781811286.

Melling, H., P. H. Johnston, and D. A. Riedel, 1995: Measurements of the underside topography of sea ice by moored subsea sonar. *J. Atmos. Oceanic Technol.*, **12**, 589–602, https://doi.org/10.1175/1520-0426(1995)012<0589:MOTUTO>2.0.CO;2.

Nansen, F., 1902: The oceanography of the North Polar Basin. *The Norwegian North Polar Expedition 1893–1896: Scientific Results*, Vol. 3, Kristiania, 427 pp.

Ninnis, R. M., W. J. Emery, and M. J. Collins, 1986: Automated extraction of pack ice motion from Advanced Very High Resolution Radiometer imagery. *J. Geophys. Res.*, **91**, 10 725–10 734, https://doi.org/10.1029/JC091iC09p10725.

Park, H. S., A. L. Stewart, and J. H. Son, 2018: Dynamic and thermodynamic impacts of the winter Arctic Oscillation on summer sea ice extent. *J. Climate*, **31**, 1483–1497, https://doi.org/10.1175/JCLI-D-17-0067.1.

Raffel, M., C. E. Willert, F. Scarano, C. J. Kähler, S. T. Wereley, and J. Kompenhans, 2018: *Particle Image Velocimetry*. 2nd ed. Springer, 669 pp., https://doi.org/10.1007/978-3-319-68852-7.

Rollenhagen, K., R. Timmermann, T. Janjić, J. Schröter, and S. Danilov, 2009: Assimilation of sea ice motion in a finite-element sea ice model. *J. Geophys. Res.*, **114**, C05007, https://doi.org/10.1029/2008JC005067.

Spreen, G., R. Kwok, and D. Menemenlis, 2011: Trends in Arctic sea ice drift and role of wind forcing: 1992–2009. *Geophys. Res. Lett.*, **38**, L19501, https://doi.org/10.1029/2011GL048970.

Stark, J. D., J. Ridley, M. Martin, and A. Hines, 2008: Sea ice concentration and motion assimilation in a sea ice-ocean model. *J. Geophys. Res.*, **113**, C05S91, https://doi.org/10.1029/2007JC004224.

Sumata, H., T. Lavergne, F. Girard-Ardhuin, N. Kimura, M. A. Tschudi, F. Kauker, M. Karcher, and R. Gerdes, 2014: An intercomparison of Arctic ice drift products to deduce uncertainty estimates. *J. Geophys. Res. Oceans*, **119**, 4887–4921, https://doi.org/10.1002/2013JC009724.

——, R. Gerdes, F. Kauker, and M. Karcher, 2015: Empirical error functions for monthly mean Arctic sea-ice drift. *J. Geophys. Res. Oceans*, **120**, 7450–7475, https://doi.org/10.1002/2015JC011151.

Thorndike, A. S., and R. Colony, 1982: Sea ice motion in response to geostrophic winds. *J. Geophys. Res.*, **87**, 5845–5852, https://doi.org/10.1029/JC087iC08p05845.

Tschudi, M. A., C. Fowler, J. Maslanik, and J. Stroeve, 2010: Tracking the movement and changing surface characteristics of Arctic sea ice. *IEEE J. Sel. Top. Appl. Earth Obs. Remote Sens.*, **3**, 536–540, https://doi.org/10.1109/JSTARS.2010.2048305.

——, W. N. Meier, and J. S. Stewart, 2020: An enhancement to sea ice motion and age products at the National Snow and Ice Data Center (NSIDC). *Cryosphere*, **14**, 1519–1536, https://doi.org/10.5194/tc-14-1519-2020.

Valkonen, E., J. Cassano, and E. Cassano, 2021: Arctic cyclones and their interactions with the declining sea ice: A recent climatology. *J. Geophys. Res. Atmos.*, **126**, e2020JD034366, https://doi.org/10.1029/2020JD034366.